Velocity-field based load estimation of an unsteady actuator disc

Yu, Wei; Ferreira, Carlos Simao

DOI
10.1088/1742-6596/2767/2/022025

Publication date
2024

Document Version
Final published version

Published in
Journal of Physics: Conference Series

Velocity-field based load estimation of an unsteady actuator disc

Journal of Physics: Conference Series **2767** (2024) 022025 doi:10.1088/1742-6596/2767/2/022025

Velocity-field based load estimation of an unsteady actuator disc

Wei Yu[1], **and Carlos Simao Ferreira**[1]

[1] Faculty of Aerospace Engineering, Delft University of Technology, Delft, The Netherlands

E-mail: w.yu@tudelft.nl

Abstract. Traditional methods for determining the load of an object in unsteady cases, such as Control-volume Momentum Integration (CMI) and Noca methods, encounter challenges related to near-body acceleration and pressure estimation. This prompts the need for innovative techniques to overcome these limitations. This study introduces a novel vorticity-based approach to expand classical load determination methods. The numerical results of an unsteady actuator disc (AD) CFD simulation are used to verify and quantify the uncertainty of the three methods. In the AD model, the load is prescribed and used as a source term. The velocity and pressure fields are solved from the Navier-Stokes equations using the open-source CFD package OpenFOAM, which offers a robust validation framework. Systematic examination of the robustness and accuracy of the three methods across various load and motion unsteady scenarios reveals that the proposed vorticity-based method excels in steady-state scenarios, exhibiting the highest level of robustness and accuracy. In contrast, the traditional CMI method proves more robust and accurate in pure motion cases. In scenarios involving static and moving AD with load variations, the new vorticity-based method demonstrates superior robustness and accuracy, mainly when moderate vorticity dynamics. Conversely, in cases with increased vorticity dynamics in the wake, the accuracy of the vorticity-based method decreases, with the CMI method showing superiority.

1. Introduction and Objectives

In many fluid dynamic problems, it's challenging and sometimes even impossible to directly obtain the instantaneous aerodynamic or hydrodynamic forces on a moving body from measured or simulated data. The accuracy of force measurements, often determined through balances, faces significant interference from support structures, especially in unsteady cases [1]. In specific numerical simulations, the forces acting on an object are unavailable directly. This is evident in geometry-resolved Computational Fluid Dynamics (CFD), vortex panel modelling relying on imposed boundary conditions, and dynamic fluid-structure interaction simulations. Under such conditions, load estimation from the resolved flow field provides a solution. Load estimation from the flow field dates back to the wake-rake method [2] used for steady or mean drag estimation of a body, where only a wake-plane survey is needed. van Oudheusden et al. [3, 4] detailed how to first obtain the pressure field from the velocity field by combining the experimental data with fluid governing Navier-Stokes equations and then determine the steady or mean force based on the velocity and pressure field for incompressible and compressible flow using CMI method. Wu et.al. [1] extended CMI to unsteady incompressible flow and verified it by numerical tests of a fishlike swimming body.

However, the CMI method requires the determination of the pressure field first. Instead, Noca [5, 6] proposed an expression using a flux equation to determine the force of a moving body, which only requires the velocity field and its derivative over the contour surfaces. The

challenge in unsteady load determination is relevant for wind turbines. Examples are dynamic stall at the airfoil scale; blade rotation at operation condition, blade pitch motion at the blade scale, dynamic inflow and yaw, and the platform surge, pitch, and yaw motions of floating offshore wind turbines (FOWTs) at the rotor scale. Using the Noca method to estimate the unsteady loads of an airfoil in dynamic stall [7] and a pitching blade [8] of VAWT based on PIV-measured velocity field has been demonstrated. The Noca method has also been applied for the load determination of HAWT blades in uniform and static yaw [9]. Rival et. al. [10] compared CMI and Noca methods for an unsteady incompressible flow, identifying challenges such as near-body acceleration treatment and pressure estimation on outer surfaces of control volumes, signaling the need for new techniques to address these limitations.

This study introduces a new vorticity-based method for assessing unsteady loads acting on a body subjected to unsteady load conditions. The proposed method is compared with the two existing instantaneous load determination approaches applied to moving bodies, namely, the CMI and Noca. A series of unsteady AD-CFD simulations are conducted to validate the three methods. The study quantifies the sensitivity associated with these methods for an AD subjected to different combinations of loads and motions.

2. Load determination Methods

2.1. Control-volume Momentum Integration

In the CMI method, the initial step involves determining the pressure from the velocity field. Subsequently, the forces are derived by integrating the flow governing equation, precisely the Euler equation in this paper, based on the velocity and the determined pressure fields.

The fluid is assumed to be incompressible, inviscid, and homogeneous. Viscous stress plays a minor role compared to pressure forces along a contour far from the body surface [9]. The motion of the fluid can be described by the Euler equation

$$\rho\left(\frac{\partial \boldsymbol{u}}{dt} + \boldsymbol{u}\cdot\nabla\boldsymbol{u}\right) = -\nabla p + \boldsymbol{f} \tag{1}$$

where $\boldsymbol{u}$ is the velocity, $\boldsymbol{f}$ is the force density distribution that the body acts on the flow, ρ is the fluid density and p is the static pressure. Based on the measured velocity field and estimated pressure field in section 2.1.1, the force can be calculated from Eq. 1. The control volume of the flow used for the momentum integral is illustrated in Fig. 1. Within the control volume, the integral form for force calculation is

$$\boldsymbol{F}(t) = -\rho\iiint_{CV}\frac{\partial \boldsymbol{u}}{\partial t}dV - \rho\iint_{CS}\boldsymbol{u}\left(\boldsymbol{u}\cdot\boldsymbol{n}\right)dS - \iint_{CS}p\boldsymbol{n}dS \tag{2}$$

where CS is the control surface of the bounded control volume CV. For a fixed control volume in this method, the Leibnitz integral theorem can be applied to the time-dependent term of Eq. 2 as Eq. 3 [10].

$$-\rho\iiint_{CV}\frac{\partial \boldsymbol{u}}{\partial t}dV = -\rho\frac{\partial}{\partial t}\iiint_{CV}\boldsymbol{u}dV \tag{3}$$

The volume integral in Eq. 3 requires information in the entire control volume. This is often not the case in real applications. For example, the reflection on the body of PIV measured data. Based on the assumption of incompressible flow and applying Gauss's theorem, the volume integration of Eq. 3 is transformed into surface integration as follows [11]

$$-\rho\frac{\partial}{\partial t}\iiint_{CV}\boldsymbol{u}dV = -\rho\frac{\partial}{\partial t}\iint_{CS}\boldsymbol{x}\left(\boldsymbol{u}\cdot\boldsymbol{n}\right)dS \tag{4}$$

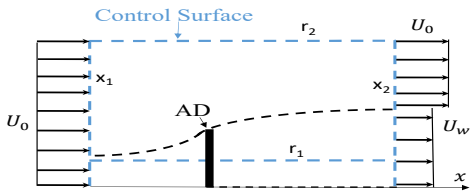

Figure 1: Illustration of the control surface used in the three load determination methods. Note: r_1 is overlapped with the x axis (the center axis of the AD) for CMI and Noca methods.

where $\boldsymbol{x}$ is the position vector of the control surface in the reference frame.

Substitute Eq. 4 into Eq. 2, the final expression for unsteady force of an arbitrary body in incompressible and inviscid flow using the momentum integration is [11, 9, 10]:

$$\boldsymbol{F}(t) = -\rho \frac{\partial}{\partial t} \iint_{CS} \boldsymbol{x}\,(\boldsymbol{u}\cdot\boldsymbol{n})\,dS - \rho \iint_{CS} \boldsymbol{u}\,(\boldsymbol{u}\cdot\boldsymbol{n})\,dS - \iint_{CS} p\boldsymbol{n}dS \tag{5}$$

The pressure is normally determined by solving the Poisson pressure equation [12, 13, 14, 9].

2.1.1. Pressure determination The pressure field needs to be determined before calculating force. van Oudheusden [4] provided an overview of pressure determination using a PIV-based velocity field of both steady and unsteady flow. For incompressible flow, the pressure gradient can be calculated by the Navier-Stokes Momentum equation, which is given by

$$\nabla p = -\rho(\nabla \cdot \frac{\partial \boldsymbol{u}}{\partial t} + (\boldsymbol{u}\cdot\nabla\boldsymbol{u})) + \mu\nabla^2\boldsymbol{u} \tag{6}$$

where μ is the coefficient of dynamic viscosity. Taking the divergence of Eq. 6, under the assumption of incompressible($\nabla\cdot\boldsymbol{u}=0$), the equation becomes the Poisson equation

$$\nabla^2 p = -\rho\nabla\cdot(\boldsymbol{u}\cdot\nabla)\boldsymbol{u} \tag{7}$$

As noticed, the Poisson equation holds for both steady and unsteady flow as the time-dependent term, and the viscous term disappears without any other assumptions rather than incompressibility. However, the time-dependent information is needed to determine the pressure gradient. After the pressure gradient is found, the pressure can be calculated by solving the Poisson pressure equation, as employed by [12, 13, 14, 9]. It is given in Eq. 8

$$\nabla^2 p \approx Dp = g(u,v) \Rightarrow p = D^{-1}p \tag{8}$$

where the matrix D is obtained through the discretization of the Laplace operator using a second-order finite difference method, while $g(u,v)$ represents the forcing function derived from the momentum equation using the central finite difference method [9]. Subsequently, the equations can be solved by applying boundary conditions. A Dirichlet condition was applied at the upstream and disc center boundaries. In contrast, a Neumann condition was imposed at the downstream and the outer flow boundaries.

2.2. Noca method

Noca [5, 6] proposed another expression for the unsteady load force estimation of an arbitrary body in incompressible flow. This method is also based on the momentum balance of the NS

equations, but it uses flux instead of pressure. Similarly, the volume integral is transformed into the surface integral. The final closed expression is given

$$\frac{\boldsymbol{F}}{\rho} = \iint_{CS} \boldsymbol{n}\gamma_{flux} dS \tag{9}$$

where the flux term γ_{flux} is defined with the unit tensor $\boldsymbol{I}$ and viscous stress tensor $\boldsymbol{T}$ as

$$\begin{aligned}\gamma_{flux} = \frac{1}{2}\boldsymbol{u}^2\boldsymbol{I} - \boldsymbol{u}\boldsymbol{u} - \frac{1}{N-1}\boldsymbol{u}\left(\boldsymbol{x}\cdot\boldsymbol{\Omega}\right) + \frac{1}{N-1}\boldsymbol{\Omega}\left(\boldsymbol{x}\cdot\boldsymbol{u}\right) - \\ \frac{1}{N-1}\left[\left(\boldsymbol{x}\cdot\frac{\partial\boldsymbol{u}}{\partial t}\right)\boldsymbol{I} - \boldsymbol{x}\frac{\partial\boldsymbol{u}}{\partial t} + (N-1)\frac{\partial\boldsymbol{u}}{\partial t}\boldsymbol{x}\right] + \frac{1}{N-1}\left[\boldsymbol{x}\cdot\left(\nabla\cdot\boldsymbol{T}\right)\boldsymbol{I} - \boldsymbol{x}\left(\nabla\cdot\boldsymbol{T}\right)\right] + \boldsymbol{T}\end{aligned} \tag{10}$$

2.3. Vorticity-based method

The motion of the fluid particles around an AD is governed by the Euler equation and the continuity equation for an incompressible, inviscid fluid. The vorticity generated by the non-conservative force field [15], is given by

$$\frac{1}{\rho}\nabla\times\boldsymbol{f} = \frac{D\boldsymbol{\omega}}{Dt} - (\boldsymbol{\omega}\cdot\nabla)\boldsymbol{u} \tag{11}$$

In steady case, the first term on the right-hand of Eq. 11 goes to zero, implying constant total vorticity within the control volume. The force can be integrated on the control surfaces as

$$\frac{\boldsymbol{F}}{\rho} = -\iint_{CS}(\boldsymbol{\omega}\cdot\nabla)\boldsymbol{u}dS \tag{12}$$

For unsteady cases, the integrated force is

$$\frac{\boldsymbol{F}}{\rho} = \iint_{CS}\frac{D\boldsymbol{\omega}}{Dt}dS - \iint_{CS}(\boldsymbol{\omega}\cdot\nabla)\boldsymbol{u}dS \tag{13}$$

where the first term on the right denotes the total change in vorticity within the control volume, while the second term represents the exchange of vorticity flux across the control surfaces. The thrust coefficient of the AD in all three methods can be calculated from its definition $C_t = \frac{F_x}{\rho A U_0^2/2}$, where Fx is the normal force on the disc, and U_0 is the undisturbed wind speed.

3. Validation simulation setup

3.1. Actuator Disc model

To validate the three methods, the flow field of an actuator disc (AD) [16] is computed by modifying the 3D AD model in OpenFOAM [17]. The prescribed thrust coefficient is realized by imposing uniformly distributed volume forces over the AD region. The unsteady RANS was chosen to capture the unsteady features of the simulated unsteady flow. As recommended by [18], the wind turbine wakes can be studied by the AD method combined with the $k-\epsilon$ turbulence model. An ambient turbulence intensity of 0.1% is selected for the simulations.

The computational domain is set at $Y_{inlet} = 6D$, $Z_{inlet} = 6D$, $X_{upstream} = 9.2D$ and $X_{downstream} = 10D$ after a domain independence study, which is depicted in Fig. 2a. The mesh is refined at five levels, densest near the actuator disc and gradually coarser away from it. The smallest cell size is $0.002D$, while the coarsest is $0.07D$. The simulation boundary conditions consist of a velocity condition at the inlet, a pressure condition at the outlet, and a slip-wall condition on the remaining boundaries of the domain. Fig. 2b verifies the axial induction factor from the AD-CFD simulations against momentum theory with Glauert correction for steady uniform thrust ranging from $C_t = 0.2$ to $C_t = 1.3$. It shows the CFD model agrees with momentum theory with Glauert correction up to $C_t = 1.1$, the discrepancy becomes larger for $C_t = 1.2$ and 1.3. However, it is still acceptable considering the challenging high load.

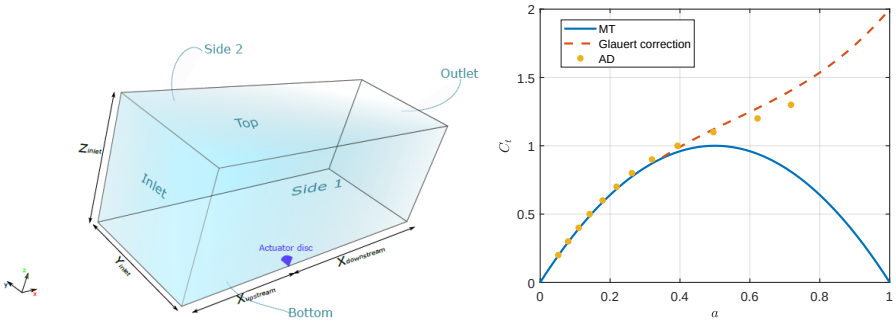

(a) Simulation domain schematic.

(b) Axial induction factor a against C_t from momentum theory with Glauert correction and AD-CFD simulations.

Figure 2: The actuator disc CFD simulation setup and its verification

3.2. Load cases

The platform of FOWTs experiences multi-degree-of-freedom motions, with surge translation being particularly significant for understanding its aerodynamics. Surge motion induces unsteady loads on the rotor, posing a challenge for accurate load estimation, especially in wind tunnel tests and blade-resolved CFD simulations. It's essential to decouple motion effects from load variation effects on the rotor to address the effect of different factors. This is achieved by simulating AD with harmonic motion, harmonic varying loads, and their coupled effects.

Therefore, in addition to steady scenarios, three types of unsteady load cases are simulated to evaluate the efficacy of the three load estimation methods. In the first type, the AD is only imposed harmonic variation of thrust, C_t is prescribed by

$$C_t = C_{t0} - A_{C_t} cos(\frac{f_{red} U_0}{D} t) \tag{14}$$

The second type only imposes the AD to harmonic translational motion. The translational motion is prescribed by

$$x = x_0 + A_x sin(\frac{f_{red} U_0}{D} t) \tag{15}$$

where f_{red} is the reduced frequency of the load variation or the translational motion, defined by $f_{red} = \frac{fD}{U_0}$; C_{t0} and x_0 is the initial steady state baseline thrust coefficient or initial axial position of the AD; A_{C_t} and A_x are the amplitude of thrust or translation position variations; U_0 and D are the incoming wind speed and the diameter of the disc, respectively.

In the third type, the AD is simultaneously imposed on harmonic thrust variation and harmonic translational motion. The harmonic force and the translational motion are prescribed by Eq. 14 and Eq. 15, respectively. Two different C_{t0} and two different frequencies were chosen. The selected tested load cases are summarized in Table 1.

4. Results

This section conducts a comparative analysis, juxtaposing the loads determined by the three methods against the actual load applied to the AD in the CFD simulation for load cases detailed in section 3.2. To initiate the assessment, a sensitivity analysis is performed first, scrutinizing the impact of boundary size through a one-variable-at-a-time method, for all cases.

Table 1: Simulated steady and unsteady load cases.

Case	A1	A2	B1	B2	C1	C2	D1	D2
C_{t0}	0.8	0.5	0.8	0.8	0.8	0.8	0.8	0.8
A_{C_t}	0	0	0.5	0.5	0	0	0.5	0.5
A_x	0	0	0	0	0.1D	0.1D	0.1D	0.1D
f_{red}	-	-	1	10	1	10	1	10

4.1. Steady actuator disc

Fig. 3 presents the relative difference in estimated C_t compared to the reference C_t when employing different control contours outlined in Fig. 1 for the three methods. In the vorticity-based method, vorticity is only generated where the pressure gradient is non-zero, specifically at the disc's edge. Consequently, the technique permits selecting a control volume focused on the disc region, eliminating the need to cover the entire disc area. In contrast, both momentum balance-based methods of Noca and CMI require aligning the inner radial boundary with the disc's x-axis to ensure complete inclusion of the AD within the integral control volume.

As shown in Fig. 3a, the vorticity-based method demonstrates robustness when the inner boundary avoids intersecting with the primary vorticity sheet shed at the disc edge ($r1/D < 0.48$). Consequently, a fixed inner boundary ($r1 = 0.4D$) is selected for all unsteady cases. In Fig. 3b, it is evident that both the vorticity-based and Noca methods are sensitive to the choices of control surfaces when the outer boundary interferes with the vorticity sheet ($r2/D < 0.64$). Robustness is achieved as long as the boundaries remain clear of the vortex sheet. Fig. 3c illustrates that when the upstream boundary does not interfere with the disc ($x_1/D < -0.05$), the proposed vorticity-based method demonstrates the most robust results with the highest accuracy. Conversely, the error estimated by the CMI method increases with the increase in the upstream boundary size (x_1). The Noca method also proves robust against varying boundaries, exhibiting an accuracy level between the former two methods. Fig. 3d exhibits an opposite trend for the CMI method while a similar trend for the vorticity-based method to the upstream boundary in Fig. 3c. The vorticity-based method shows a very robust estimation with almost no variation to the varying size of the downstream boundary (x_2), while the error estimates by the CMI method decrease as the increase of the distance of downstream boundary. This is because the further the wake is included in the control volume, the less momentum loss for the momentum-balance-based methods of CMI and Noca, though the varying range of the Noca method is more minor. However, around a distance of $x_2/D = 1.5$, as indicated by Fig. 7a, wake mixing starts in the wake shear layer, leading to fluctuations in the estimated loads. Hence, the maximal downstream distance of $x_2/D = 1.6$ is used for all subsequent cases.

In summary, the proposed vorticity-based method, focusing on the generated vorticity near the disc edge, proves the most robust to boundary selections, provided the inner and outer boundaries do not interfere with the vortex sheet. Boundary sizes notably influence the CMI method. The Noca method, positioned between the two approaches, integrates over a larger control surface encompassing the object than the vorticity-based method, resulting in higher errors and higher sensitivity to boundary sizes than the newly proposed vorticity-based method.

4.2. Static actuator disc with unsteady loads

The top figures of Fig. 4 compare the Root Mean Square Error (RMSE) estimated by the three methods for varying boundaries for case B. The bottom figures of Fig. 4 juxtapose the estimated time series load from the three methods with the lowest RMSE condition against the reference load imposed on the AD in the CFD simulation for load cases B1 and B2. The RMSE is

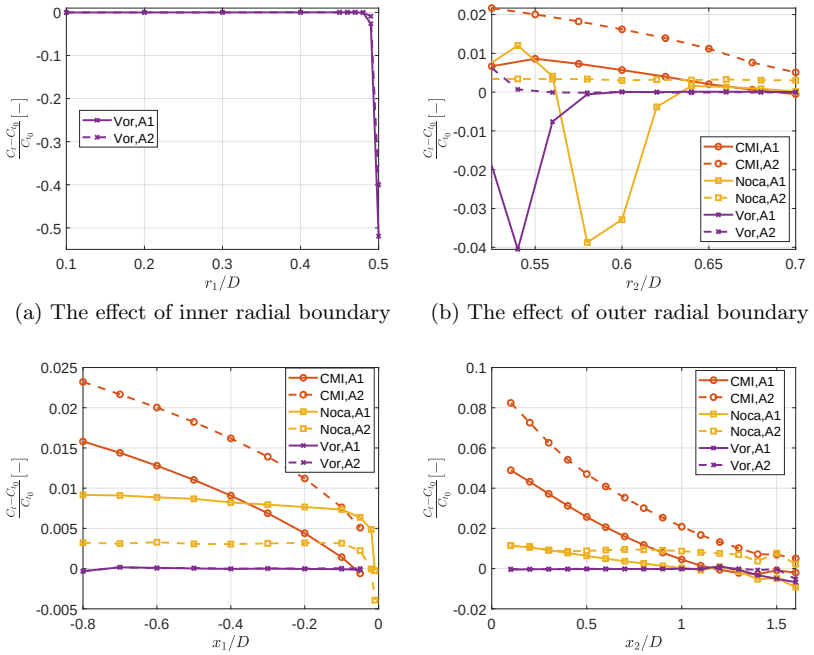

(a) The effect of inner radial boundary

(b) The effect of outer radial boundary

(c) The effect of upstream boundary

(d) The effect of downstream boundary

Figure 3: Comparison of RMS for different boundary sizes for steady cases A1 and A2

computed as $RMSE(Ct, Ct_{pres}) = \sqrt{\frac{1}{N}\sum_{i=1}^{i=N}(C_{t,estimated}(i) - C_{t,prescribed}(i)}$, where N denotes the number of phases with one period extracted from the simulation.

Fig. 7b and 7c present the instantaneous vorticity field for Cases B1 and B2, respectively. The load variation on the AD results in fluctuations in wake width, eventually leading to the initiation of vorticity sheet roll-up, as described in [19]. In Case B1 (Fig. 7b) with a lower frequency, the vorticity begins to roll up later, occurring after $x_2/D = 1.0$. Conversely, in Case B2 (Fig. 7c) with a higher frequency, the vorticity sheet initiates roll-up much earlier, around $x_2/D = 0.5$. This observation correlates with the findings in the top-left figure of Fig. 4. The errors predicted by the CMI method for Case B1 increase with the increase of x_2, while for Case B2, the predicted loads from CMI are also influenced by strong vorticity roll-up, leading to oscillations in load estimation. Both Noca and the vorticity-based methods are more sensitive to the vorticity field than the CMI method; they only demonstrate robustness in load estimation before vorticity roll-up occurs ($x_2/D < 1.0$ for Case B1 and $x_2/D < 0.5$ for Case B2). After this distance, local fluctuations in load estimation in these two methods are observed due to the local vorticity dynamics. The local fluctuations observed in the estimated load from both Noca and the vorticity-based methods in sections 4.3 and 4.4 stem from the same underlying reasons. However, the associated vorticity fields are not displayed due to space constraints.

Concerning the sensitivity of radial (r_2 in the middle of the top figures) and upstream (x_1 in the top-right figure) boundaries of Fig. 4, the findings align with those of steady cases. The vorticity-based method exhibits robustness, provided the radial boundary avoids interference with the vortex sheet ($r_2/D > 0.65$). Conversely, the CMI method demonstrates a slight increase in RMSE as the domain size expands. In case B1, characterized by moderate unsteadiness with $f_{red} = 1$, the accuracy ranking is as follows: the vorticity-based method demonstrates the highest

accuracy, followed by the Noca method and then the CMI method. Conversely, the accuracy ranking is reversed in the higher frequency case B2 with $f_{red} = 10$. Here, the strong vorticity dynamics affect the accuracy of the vorticity-based and Noca methods.

In summary, for the steady AD with varying loads in Case B, all three methods demonstrate a high estimation accuracy, achieving an RMSE within the range of 0.05 for the downstream boundary close to the disc $x_1/D = 0.1$ and the outer boundary without inferring the wake $r_2/D > 0.65$. This can also be reflected in the excellent match of the time-varying loading to the reference C_t for all the three methods in the bottom figures of Fig. 4.

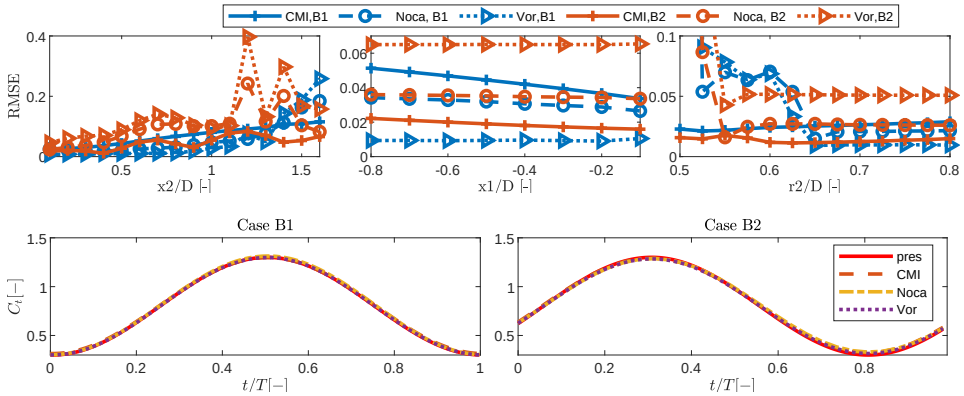

Figure 4: Comparison of the three methods for (top) control boundary sensitivity and (bottom) load estimation against actual load for steady AD with unsteady loads (Case B1 and B2).

4.3. Moving actuator disc with steady loads

Fig. 5 presents a similar comparison for load Case C, wherein a constant thrust is applied to the disc while the AD undergoes harmonic translational motion. In this pure motion scenario, CMI exhibits the highest level of robustness and accuracy. Conversely, the RMSE from the vorticity-based and Noca methods is relatively elevated, attributed to the motion-induced vorticity, particularly evident in the higher frequency case C2 ($RMSE > 0.1$ for the majority control volumes). Analyzing the estimated time series loads of the boundary with the lowest RMSE for all three methods, as depicted in the bottom figures of Fig. 5, reveals that the Noca method displays the most significant local variation for both Case C1 and C2, underscoring its sensitivity to the local vorticity field. In contrast, the CMI method provides the most robust load estimation, aligning closer with the reference load under the lowest RMSE condition. The newly proposed vorticity-based method also exhibits fluctuations in load estimation attributed to sensitivity to the vorticity field; however, these fluctuations are less pronounced than those observed with the Noca method, as demonstrated in the time series for the lowest RMSE condition. Hence, the CMI method most effectively estimates loads in pure motion cases.

4.4. Actuator disc with unsteady loads and with motions

Fig. 6 compares load case D, wherein the AD experiences simultaneous harmonic thrust variation and harmonic translational motion. In this scenario, the RMSE trends for the three methods closely resemble those observed in load case B. All three methods demonstrate a high level of accuracy in load estimation, with an RMSE within the range of 0.05 for an extensive range of control surfaces. This is also evidenced by the time series load estimation with the lowest RMSE in the bottom figures of Fig. 6. Proximity of the downstream boundary to the disc ($x_2/D = 0.2$) yields better results for all methods, and the vorticity-based method remains unaffected by upstream ($x_1 < -0.2$) and radial ($r_2 > 0.65$) boundaries. Conversely, the RMSE increases with these boundaries for the CMI method, whereas the Noca method falls between the two methods. Similar to Case B, in the moderate unsteady case D1, the vorticity-based method displays the

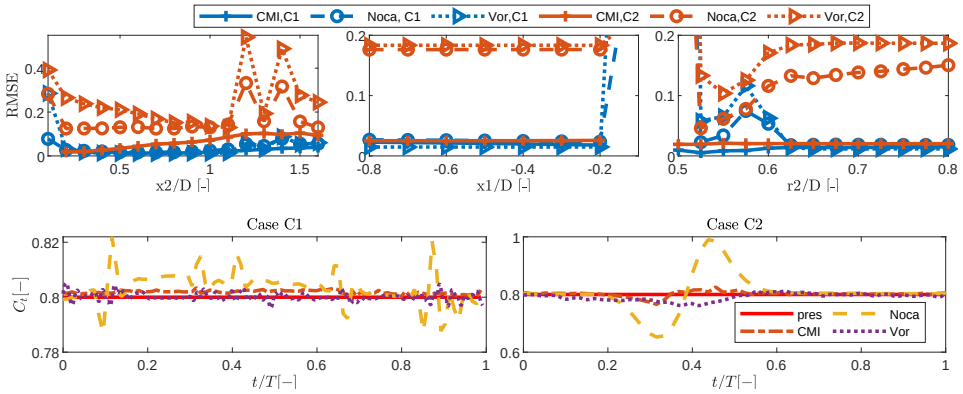

Figure 5: Comparison of the three methods for (top) control boundary sensitivity and (bottom) load estimation against actual load for moving AD with constant loads (Case C1 and C2).

highest accuracy, whereas for the higher unsteady case D2, the CMI method exhibits the highest accuracy.

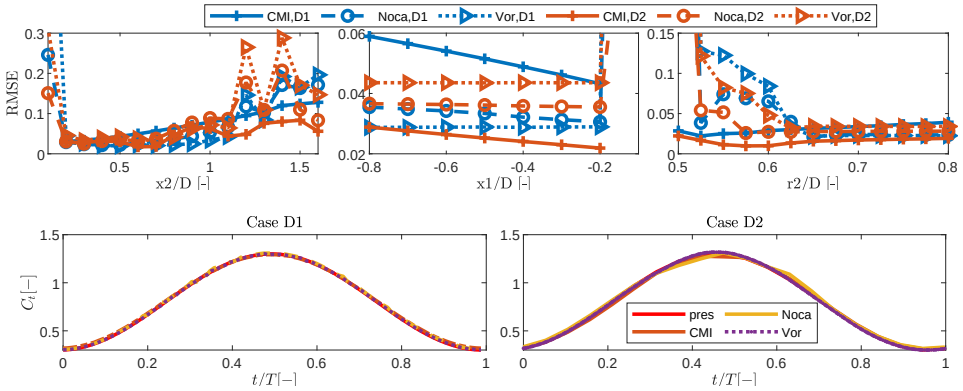

Figure 6: Comparison of the three methods for (top) control boundary sensitivity and (bottom) load estimation against actual load for moving AD with unsteady loads (Case D1 and D2).

5. Conclusions

In conclusion, we introduce a new approach for load determination from velocity fields of an unsteady actuator disc, comparing its performance with two established methods of CMI and Noca. The insights gleaned from this study shed light on the strengths and limitations of each method under different load conditions, providing valuable considerations for applying these load determination approaches in different load cases.

For steady cases, the newly proposed vorticity-based method demonstrates robustness to the choice of control boundaries, provided the boundary surface avoids interference with the vortex sheet shed from the disc's edge. In contrast, the CMI method exhibits the greatest sensitivity to the boundary size. The Noca method exhibits sensitivity to boundary sizes and accuracy levels that fall between the other two methods. Therefore, the newly proposed method is recommended for load estimation in steady-state scenarios.

In unsteady scenarios, the proximity of the downstream boundary to the disc yields better results across all methods and load cases. In cases of pure motion with constant load, the CMI method proves to be the most robust. In contrast, the other two methods are strongly affected by the vorticity induced by the motion, which introduces a high uncertainty in the estimated

load. This underscores the suitability of CMI for pure motion scenarios. For scenarios involving both static and moving actuator discs with load variations, the proposed vorticity-based method proves to be the most robust to the choices of control surfaces. Moreover, its accuracy is highest when the vorticity dynamics are not particularly strong, as seen in Case B1 and D1, making it the preferred choice for such conditions. Conversely, in cases with increased vorticity dynamics, such as in higher frequency cases like Case B2 and D2, the accuracy of the vorticity-based method decreases, and the CMI method demonstrates superiority.

Although the analysis currently overlooks viscosity effects, resulting in reduced accuracy in the far wake region where these effects become more prominent, it's notable that the viscosity effects can be included in both Noca [5] and CMI methods [9]. However, the newly proposed method currently lacks this capability. To address this limitation, future efforts will focus on establishing the relationship between the non-conservative force of viscosity and the generation of vorticity.

Appendix: Velocity and vorticity field

Fig. 7a presents the mean axial velocity field of Case A1, revealing the onset of wake mixing approximately at $x/d = 1.5$ within the shear layer. Fig. 7b and 7b show the instantaneous vorticity field of Case B1 and B2, respectively. It is observed that the vorticity sheet begins to roll up in the wake. In Case B1 (Fig. 7b), this occurs later around $x/D = 1.0$ for the lower frequency case, whereas in Case B2 (Fig. 7c), it happens earlier at $x/D = 0.5$ for the higher frequency case.

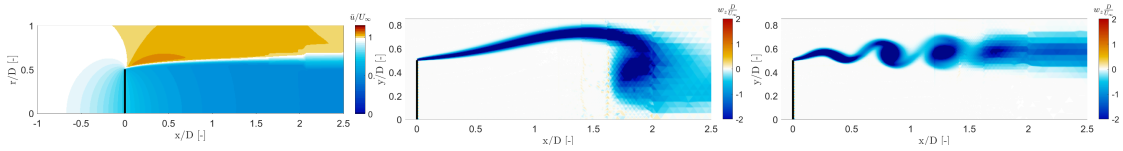

(a) Case A1 (b) Case B1 (c) Case B2

Figure 7: (a) Axial velocity field of Case A1; Vorticity field of (b) Case B1 and (c) Case B2

References

[1] Wu J Z, Pan Z L and Lu X Y 2005 *Physics of Fluids* **17** 1–4 ISSN 10706631
[2] Betz A 1925 *NACA Technical Note 337*
[3] van Oudheusden B, Scarano F, Roosenboom E, Casimiri E and Souverein L 2007 *Experiments in Fluids* **43** 153–162 ISSN 07234864
[4] van Oudheusden B 2013 *Measurement Science and Technology* **24** 1–32
[5] Noca F, Shiels D and Jeon D 1997 *Journal of Fluids and Structures* **11** 345–350
[6] Noca F, Shiels D and Jeon D 1999 *Journal of Fluids and Structures* **13** 551–578
[7] Ferreira C J, van Bussel G, van Kuik G and Scarano F 2011 *Journal of Solar Energy Engineering, Transactions of the ASME* **133**
[8] LeBlanc B and Ferreira C 2021 *Wind Energy* ISSN 10991824
[9] del Campo V, Ragni D, Micallef D, Akay B, Diez F and Ferreira C J 2014 *Wind Energy* **17** 1645–1657 ISSN 1099-1824
[10] Rival D E and van Oudheusden B 2017 *Experiments in Fluids* **58** ISSN 1432-1114
[11] Mohebbian A and Rival D E 2012 *Experiments in Fluids* **53** 319–330 ISSN 07234864
[12] van Oudheusden B, Casimiri E and Scarano F 2008 *The Aeronautical Journal*
[13] Souverein L, van Oudheusden B and Scarano F 2007 *45th AIAA Aerospace Sciences Meeting and Exhibit*
[14] Ragni D, van Oudheusden B and Scarano F 2011 *Experiments in Fluids* **51** 361–371 ISSN 07234864
[15] Van Kuik G A 2022 *Journal of Fluid Mechanics* **941** 1–17 ISSN 14697645
[16] Sørensen J N and Shen W Z 2002 *Journal of Fluids Engineering* **124** 393 ISSN 00982202
[17] Svenning E 2010 *OpenFOAM Technical Report*
[18] Ren H, Zhang X, Kang S and Liang S 2019 *Energies* **12** ISSN 1996-1073
[19] Yu W, Ferreira C and van Kuik G 2019 *Renewable Energy* **132** 1402–1414 ISSN 0960-1481